


Article

# Structural Characteristics of Corrugated Steel Inner Walls in Liquefied Natural Gas Ship Membrane Compartments

Fengming Du <sup>1</sup>, Yuhong Zhang <sup>1</sup>, Zetian Mi <sup>2</sup> and Pan Gao <sup>3,\*</sup> 

<sup>1</sup> Key Laboratory of Ship-Machinery Maintenance & Manufacture, Dalian Maritime University, Dalian 116000, China; dfm@dlnu.edu.cn (F.D.); 15123538433@163.com (Y.Z.)

<sup>2</sup> College of Information Science and Technology, Dalian Maritime University, Dalian 116000, China; mizetian@dlnu.edu.cn

<sup>3</sup> College of Ocean Science and Engineering, Shanghai Maritime University, Shanghai 201306, China

\* Correspondence: pgao@shmtu.edu.cn; Tel.: +86-21-38284800

**Abstract:** Under high sea conditions, liquefied natural gas (LNG) ships undergo significant shaking, which can affect the deformation and stress levels in the membrane tank walls. In this work, the structural characteristics of the corrugated steel inner wall in LNG ship membrane tanks were examined, different finite element models were established, and the structural characteristics under normal conditions, high sea conditions, and defective conditions were evaluated. The results revealed that corrugated steel exhibited high stress and strain under high sea conditions, with early signs of initial yield. In the presence of defects, the corrugated steel strip experienced higher stress and strain under the same load. Particularly, at a pressure of 10 bar, the defective corrugated steel exhibited a 2.3% increase in maximum stress than the defect-free corrugated steel. Additionally, the incorporation of reinforcement into the corrugated plate significantly reduced its stress and strain. Under a pressure of 10 bar, the reinforced corrugated plate exhibited a maximum stress of 503 MPa, which was 5.1% lower than that of the non-reinforced corrugated plate. This study provides theoretical support and guidance for designing and optimizing the inner wall structure of LNG ship membrane tanks.

**Keywords:** LNG ship; corrugated steel; structural characteristic



**Citation:** Du, F.; Zhang, Y.; Mi, Z.; Gao, P. Structural Characteristics of Corrugated Steel Inner Walls in Liquefied Natural Gas Ship Membrane Compartments. *J. Mar. Sci. Eng.* **2024**, *12*, 1987. <https://doi.org/10.3390/jmse12111987>

Academic Editor: Vincenzo Crupi

Received: 13 September 2024

Revised: 11 October 2024

Accepted: 27 October 2024

Published: 4 November 2024



**Copyright:** © 2024 by the authors. Licensee MDPI, Basel, Switzerland. This article is an open access article distributed under the terms and conditions of the Creative Commons Attribution (CC BY) license (<https://creativecommons.org/licenses/by/4.0/>).

## 1. Introduction

The global liquefied natural gas (LNG) trade is expanding rapidly; meanwhile, the demand for carbon reduction is growing, which has increased the market demand for LNG ships. The liquid cargo containment system is one of the three core systems of LNG ships, specifically designed to protect liquid cargo. This system consists of primary and secondary barriers, an insulation layer, a space between the barriers, and key adjacent structures that support these components [1–4]. The liquid tank enclosure system has evolved into various forms, and traditional LNG cargo tanks typically utilize membrane-type, MOSS-spherical type, and independent designs. Compared with other membrane containment systems, the MARK-III membrane containment system provides a shorter construction cycle, lower production costs, superior structural performance, enhanced low-temperature resistance, and reduced cargo evaporation rate. These advantages make this membrane system a crucial component of LNG ship liquid cargo containment systems. The maintenance of membrane-type enclosure systems is more complex and costly compared with other systems used on ship hulls. The sea conditions are divided into 10 levels, and sea conditions above level 5 are called high sea conditions. Under high sea conditions, the waves are very high and the ship will sway violently. LNG tank oscillation will generate significant oscillation pressure on the inner wall of the membrane tank, causing uneven pressure on the corrugated steel. Moreover, defects such as damage or cracks in the containment system pose significant risks to both the ship hull and the safety of the crew. Therefore,

investigating the structural characteristics of the MARK-III membrane enclosure system is crucial [5–15].

Numerous scholars have investigated LNG containment systems [16–21]. Ju et al. [22] examined the effect of water elasticity on the safety of the liquid tank enclosure system in the LNG ship. The results revealed that water elasticity significantly affected the sloshing load of the liquid tank. Additionally, the study introduced correction coefficients and empirical formulas to account for the effects of water elasticity on the containment system. Wu et al. [23] compared the pressure differences in the cargo hold of a 220,000 m<sup>3</sup> membrane-type LNG ship through the two-dimensional and three-dimensional acceleration ellipse methods. The effect of the transverse stability center height of the ship on the pressure within the cargo hold was analyzed. Fu et al. [24] investigated the relationship between the pressure acting on ship cargo tanks and various parameters such as ship length and width. By calculating the internal pressure of LNG cargo tanks, these authors developed a dimensionless pressure distribution map for the internal pressure along the tank boundaries. Kim et al. [25] investigated the pressure resistance of thin film cabin stainless steel molds through experimental simulations and finite element modeling and proposed methods to enhance their performance. Sohn et al. [26] used a finite element model to determine the yield strength of stainless steel film and analyze its structural response under oscillatory loading. Park et al. [27] used artificial intelligence to predict the ultimate buckling strength of the liquid cargo containment system in the LNG ship under sloshing loads. Moreover, the ANN method was effectively used to identify the relationship between complex inputs and outputs related to the cargo system. This analysis was applied to simulate and calculate the ultimate buckling strength of the GTT NO96 liquid cargo containment system under sloshing loads. Graczyk et al. [28] performed pressure measurements while accounting for temporal and spatial distribution. They presented an experimental approach applied by MARINTEK for analyzing sloshing phenomenon. The local pressure effects were discussed based on low filling level tests with different wall surfaces. Yan et al. [29] calculated the SIF of a crack in a ship detail by combining a PATRAN finite element model for the whole ship with the advantages of ANSYS for SIF calculation, incorporating a macrocode written to achieve the transformation. The method was validated by comparison with existing empirical formulas. Dong et al. [30] presented a probabilistic framework for fatigue risk and updating assessments through inspection events. The computation associated with fatigue damage was performed using fracture mechanics and uncertainties are considered within this process.

Although scholars have conducted many studies on LNG membrane compartments, there are still limited studies on the structural characteristics of corrugated steel under high sea conditions, and there are few reports on how to improve the safety of membrane storage structures. Currently, no research has been conducted on the structural safety of MARK-III membrane cabin walls with specific defects under high sea conditions.

In this work, corrugated steel inner walls of MARK-III membrane compartments were examined and the response of the corrugated steel inner wall structure under normal conditions, high sea conditions, and defective conditions was analyzed. This work provides theoretical support and guidance for designing and optimizing the inner wall structure of LNG ship membrane compartments.

## 2. Model Description

The main shielding film of the MARK III liquid cargo enclosure system consists of 304 L stainless steel corrugated plates. Therefore, this paper utilizes 1.2 mm thick 304 L stainless steel corrugated plates as the research object and establishes a flat plate model with dimensions matching those of the corrugated plate model. This flat plate is attached to the bottom of the corrugated plate for analysis. The steel plate exhibits a symmetrical structure composed of a flat plate and a circular arc. The transitions between the flat plate and the slope surface and the top are designed with arcs of different curvatures (Figure 1a).

In this model, uniform pressure and non-uniform pressure are applied to simulate the normal condition and high sea condition.

In practical applications, corrugated steel may develop defects due to collisions. To simulate the effect of these defects on the response of corrugated steel structures, a cylinder with the same length as the corrugated steel is constructed. The surface of this cylinder is positioned tangentially to the middle of the corrugated plate. The defect in corrugated steel is simulated through the normal displacement of the cylinder (Figure 1b).

To improve the structural stability of corrugated steel, a reinforcement component is designed in contact with the inner surface along the length of the corrugated steel (Figure 1c).

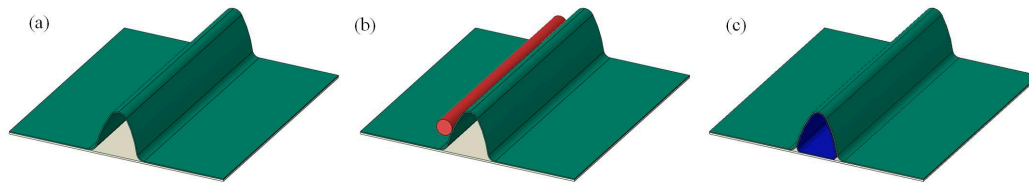


**Figure 1.** (a) Normal corrugated plate model; (b) defect model; (c) enhancement model.

### 2.1. Control Equation

The Johnson–Cook constitutive model is used to characterize the stress–strain characteristics of 304L stainless steel. The Johnson–Cook constitutive model uses a continuous multiplication relationship to describe the effects of strain, strain rate, and temperature on the constitutive stress and failure strain of materials during deformation. At present, scholars have described the mechanical behavior of various materials such as copper, steel, and titanium using the Johnson–Cook constitutive model, which has been widely applied in engineering practice. The Johnson–Cook constitutive model is expressed by the following formula:

$$\sigma = [A + B\varepsilon^n] \left[ 1 + C \ln\left(\frac{\dot{\varepsilon}}{\dot{\varepsilon}_0}\right) \right] \left[ 1 - \left( \frac{T - T_r}{T_m - T_r} \right)^m \right] \quad (1)$$

where  $A$  represents the initial yield strength,  $B$  denotes the strain strengthening index,  $n$  indicates the strain rate sensitivity index, and  $m$  signifies the temperature softening index. Based on the dynamic data of 304L stainless steel at room temperature and high temperatures, the material parameters of the Johnson–Cook constitutive model were fitted using the least squares method [31].

### 2.2. Boundary Conditions

(1) In the three models, the flat plate is treated as a rigid body and is connected to the bottom surface of the corrugated plate. The bottom plate is set as the primary surface, while the corrugated plate is designated as the secondary surface. The interaction between these two plates is modeled as a rigid connection in the normal direction. The augmented Lagrangian algorithm is selected as the contact algorithm to avoid infiltration between the corrugated steel and flat plate.

(2) Owing to the negligible displacement in the thickness direction of the corrugated steel, fixed constraints are applied to the cross-sectional edges on both sides of the model and the bottom plate.

(3) Non-uniform pressure and uniform pressure are applied to the normal corrugated plate model, respectively, as shown in Figure 2. Under high sea conditions, the swaying of LNG tanks can cause the corrugated steel to bear unilateral pressure. Therefore, non-uniform pressure on one side is used to simulate the stress state of corrugated steel under high sea conditions, as shown in Figure 2a.

(4) In the defect model, a contact pair is established between the corrugated plate and the cylindrical surface. The cylinder is treated as rigid, and normal displacement is applied

in the direction of the corrugated steel to simulate a manufacturing defect. The augmented Lagrangian algorithm is selected as the contact algorithm.

(5) In the reinforcement model, the reinforcement is defined as the primary surface, while the corrugated steel is the secondary surface. For interactions between the reinforcement and the base plate, the base plate is considered the primary surface, while the reinforcement is the secondary surface. These interactions are modeled as rigid contacts in the normal direction.

If the contact algorithm is not set, there will be a result of mutual infiltration between the flat plate and the corrugated steel in the calculation, resulting in an underestimated stress result, especially in high sea conditions with high pressure. If the fixed constraints are not applied to the cross-sectional edges on both sides of the model and the bottom plate, it will make the calculated stress value smaller. So, appropriate boundary conditions are important.

The dimensions of the model are shown in Figure 3. The calculation parameters are listed in Table 1.

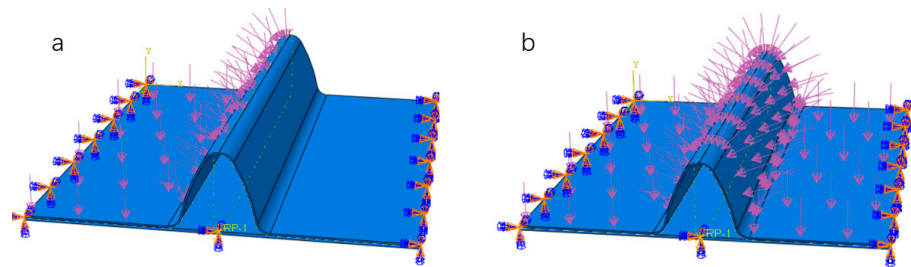


Figure 2. Diagram of (a) non-uniform pressure and (b) uniform pressure.

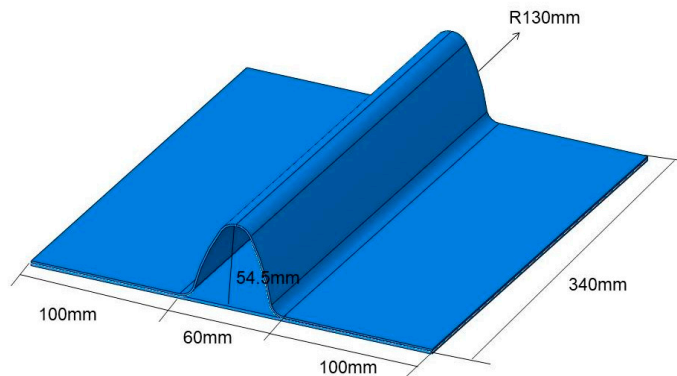


Figure 3. Dimensions of the model.

Table 1. Calculation parameters.

Item	Value
Thickness	1.2 mm
Height	54.5 mm
Length	340 mm
Yield strength	215 MPa
Tensile strength	520 MPa
Elastic modulus	193 GPa
Poisson's ratio	0.3
Pressure	1, 3, 6, 10 bar
<i>A</i>	454
<i>B</i>	1962
<i>n</i>	0.752
<i>C</i>	0.1732
<i>m</i>	0.699

The mesh convergence analysis is shown in Table 2; when the grid node is greater than 458,942, the deviation of maximum stress is very small, so it can be regarded that the number of grids has no impact on the simulation results.

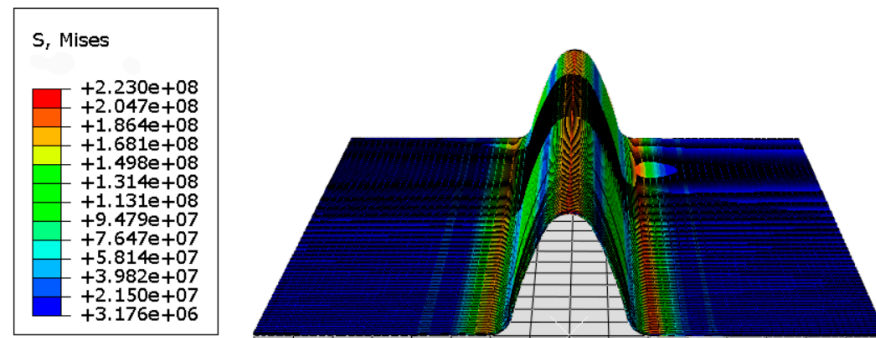
**Table 2.** Mesh convergence analysis.

Number of Grid	Maximum Stress (MPa)	Deviation
77,845	474.3	-
196,987	511.4	37.1
379,845	534.6	23.2
458,942	542.4	7.8
501,246	544.1	1.7

### 3. Results and Discussion

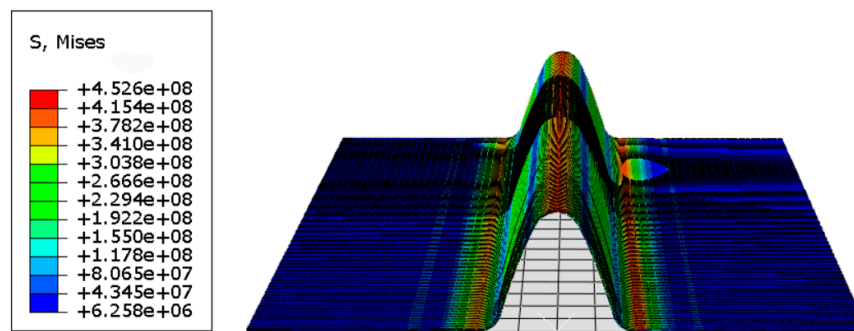
#### 3.1. Structural Response of Corrugated Steel Under Uniform Loading

Figure 4 shows the stress cloud map of corrugated steel under a uniform pressure of 3 bar. Under this pressure, the corrugated steel gradually undergoes deformation at the top and transition regions of the corrugated plate.



**Figure 4.** Stress cloud map of the model under uniform pressure of 3 bar.

Figure 5 shows the stress distribution map of the corrugated steel under a uniform pressure of 6 bar. Under this pressure, the stress on the corrugated plate further increases. However, the overall stability of the structure remains unchanged, with no plastic deformation or structural alterations.



**Figure 5.** Stress cloud map of the model under uniform pressure of 6 bar.

Figures 6 and 7 show the stress and strain cloud maps of the corrugated plate under a uniform pressure of 10 bar, respectively. At this pressure, the overall stress and strain of the corrugated plate significantly increase, leading to plastic deformation in most of the compressed areas. Consequently, the overall structure becomes unstable, collapses, and is destroyed.

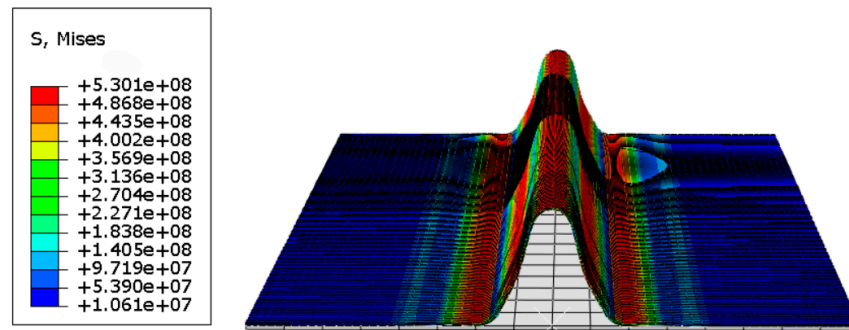


Figure 6. Stress cloud map of the model under uniform pressure of 10 bar.

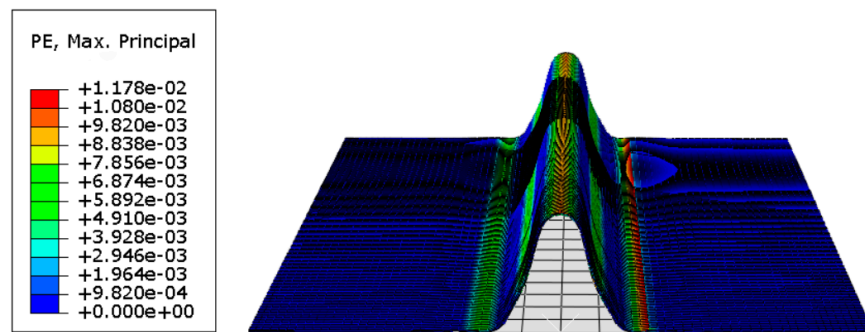


Figure 7. Strain cloud map of the model under uniform pressure of 10 bar.

Figure 8 shows the strain of the corrugated plate under different uniform loads. Under a uniform load, deformation mainly occurs in the central arc section of the corrugated plate. With increasing pressure, the curvature radius of the arc also increases. Moreover, the top of the corrugated plate undergoes minimal strain before reaching instability, with the overall strain in the model being insignificant. Upon reaching instability, the model undergoes severe deformation.

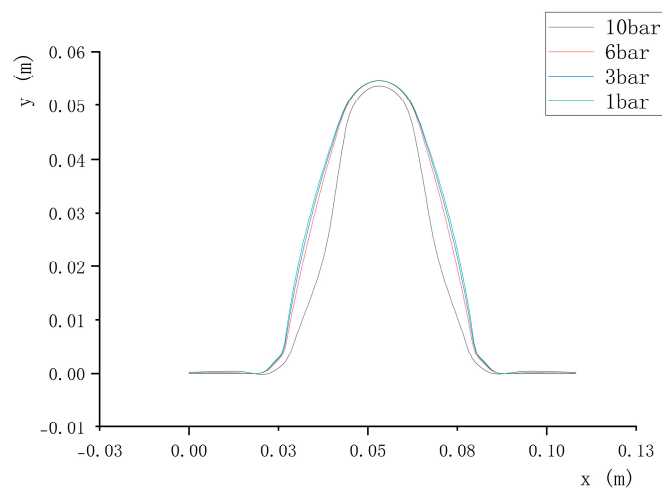


Figure 8. Strain distribution of the model under different uniform pressures.

### 3.2. Structural Response of Corrugated Steel Under High Sea Conditions

Under high sea conditions, corrugated steel will bear uneven pressure, so unilateral pressure is used to simulate the stress situation of corrugated steel under high sea conditions. Figure 9 shows the stress cloud map of the corrugated steel under non-uniform unilateral pressure of 3 bar. The corrugated steel exhibits significantly greater overall stress under unilateral pressure compared with uniform pressure. Moreover, under high sea conditions,

the stress concentration in the corrugated plate is mainly observed in the middle of the stressed side, the lower transition area of the stressed side, and the upper area of the non-stressed side. The entire corrugated plate exhibits an asymmetric stress distribution pattern. Additionally, some areas with high-stress concentration gradually deform, leading to a slight tilt of the entire model.

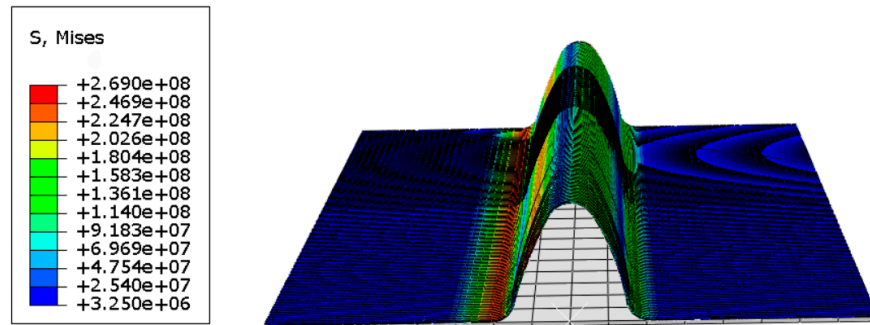


Figure 9. Stress cloud map of the model under non-uniform pressure of 3 bar.

Figure 10 shows the stress distribution of corrugated steel under a non-uniform pressure of 6 bar. Under this uneven pressure, the stress in the corrugated steel further increases, leading to localized plastic deformation. The corrugated plate exhibits significantly higher stress under this uneven pressure compared with a uniform pressure of the same magnitude.

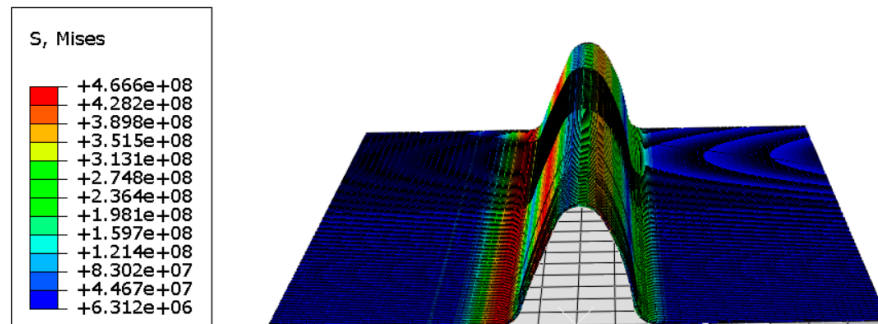


Figure 10. Stress cloud map of the model under non-uniform pressure of 6 bar.

Figures 11 and 12 show the stress and strain in the corrugated steel under a non-uniform pressure of 10 bar. Under this uneven pressure, the strain in the corrugated plate further increases, causing the model to tilt significantly toward the non-stressed side. Consequently, the entire structure becomes unstable, collapses, and loses its original form under high sea conditions.

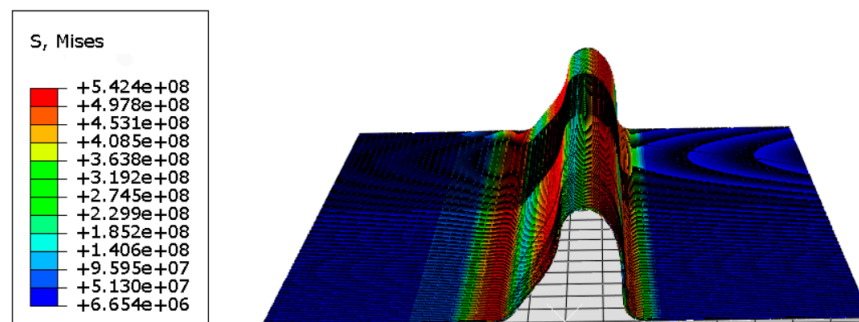


Figure 11. Stress cloud map of the model under non-uniform pressure of 10 bar.

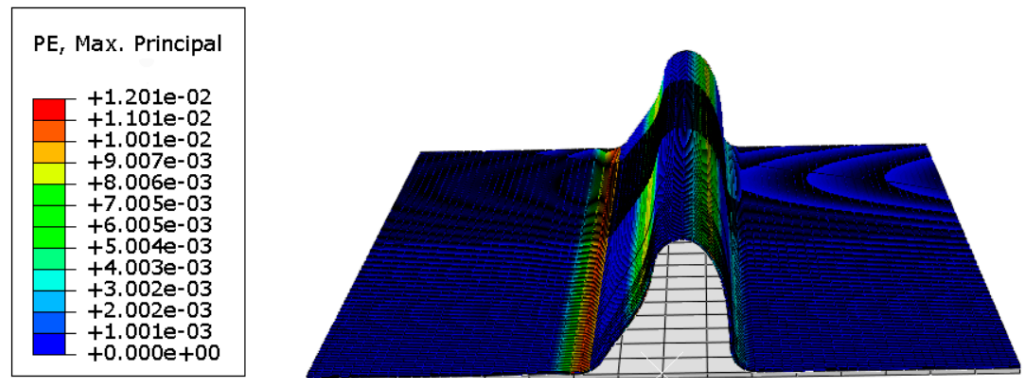


Figure 12. Plastic deformation of the model under non-uniform pressure of 10 bar.

Figure 13 shows the strain distribution of the corrugated plate under different non-uniform loads. Under high sea conditions, deformation mainly occurs in the middle, top, and transition areas below the stressed side of the corrugated plate. At loads of 1 and 3 bar, the corrugated plate exhibits minimal overall strain. However, under a load of 6 bar, the corrugated plate undergoes significant deformation, causing the model to tilt significantly toward the non-stressed side. Under a load of 10 bar, the model loses all stability. Corrugated plates under high sea conditions exhibit significantly higher strain and earlier initial yield than those under uniform loads.

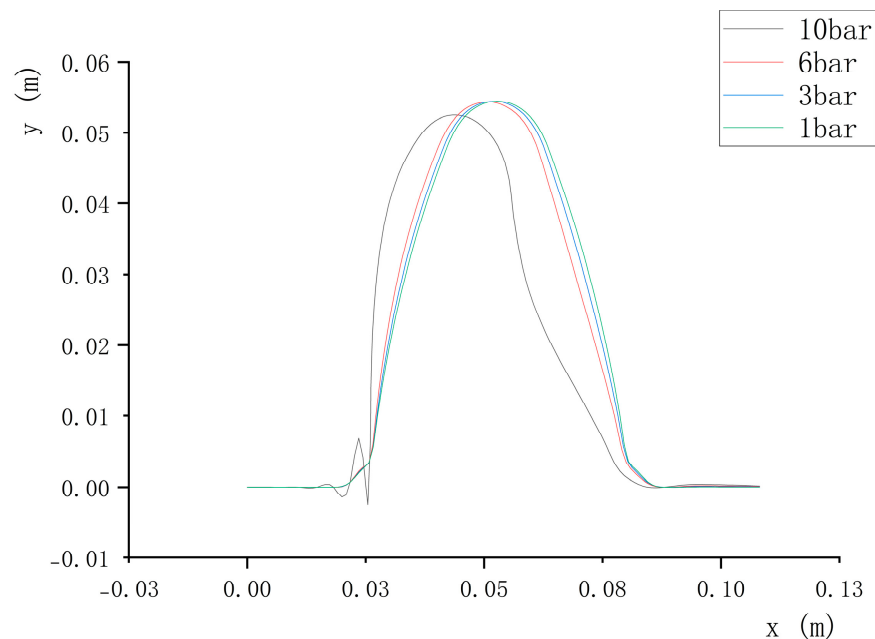


Figure 13. Strain of the model under different non-uniform pressures.

### 3.3. Structural Response of Defective Corrugated Steel Under High Sea Conditions

By creating defects through cylindrical surfaces and applying unilateral pressure, the structural response of defective corrugated steel under high sea conditions can be simulated. Figure 14 shows the stress cloud map of the corrugated steel under uneven pressure of 1 bar. At this pressure, the defective corrugated steel exhibits significantly higher stress and strain than the defect-free steel. However, the defective steel still functions effectively.



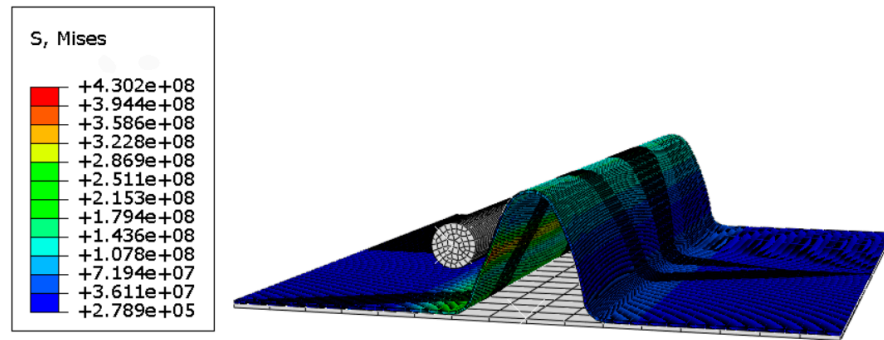


Figure 14. Stress cloud map of the defective model under non-uniform pressure of 1 bar.

Figure 15 shows the stress cloud map of the corrugated steel under a non-uniform pressure of 3 bar. Under this pressure, the defective corrugated steel exhibits higher stress and strain than the defect-free steel. Although the maximum stress at 3 bar is lower than at 1 bar, the stress is more evenly distributed across the corrugated plate.

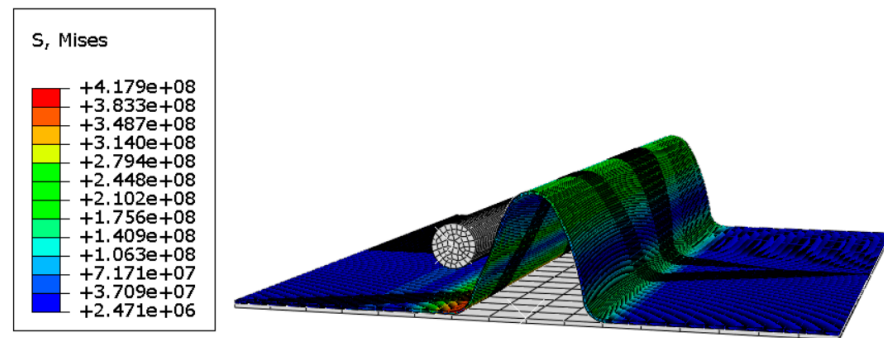


Figure 15. Stress cloud map of the defective model under non-uniform pressure of 3 bar.

Figure 16 shows the stress cloud map of the corrugated steel under a non-uniform pressure of 6 bar. Under this pressure, the stress and strain of corrugated steel further increase. Although the maximum increase in stress is relatively minimal, the overall stress in the corrugated plate significantly increases, leading to an expanded area of plastic deformation.

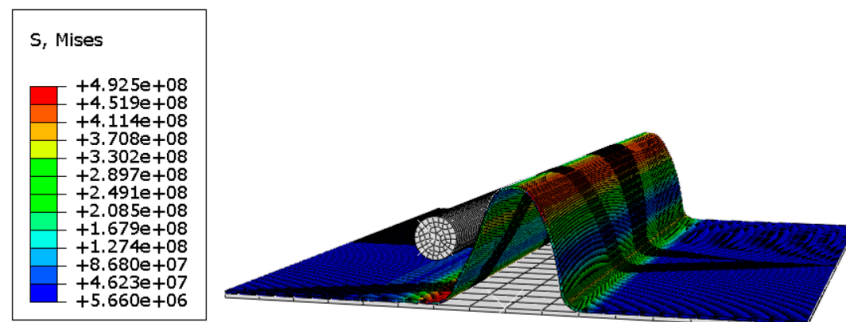


Figure 16. Stress cloud map of the defective model under non-uniform pressure of 6 bar.

Figure 17 illustrates the stress cloud map of the corrugated steel under a non-uniform pressure of 10 bar. Under this pressure, the defective corrugated steel exhibits significantly higher stress and strain and a wider stress distribution than the defect-free steel. Consequently, the overall model fails and becomes non-operational.

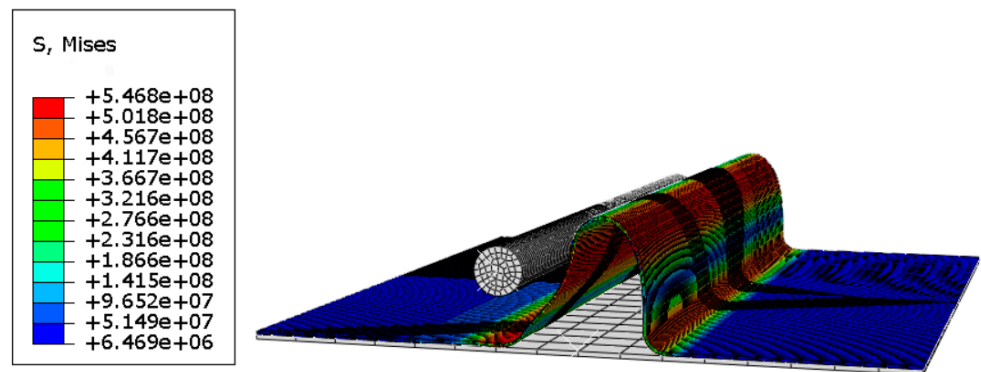


Figure 17. Stress cloud map of the defective model under non-uniform pressure of 10 bar.

Previous results reveal that under the same load, the defective corrugated steel exhibits greater stress and strain and is more prone to instability than the defect-free corrugated steel. The impact of defects on the strength of corrugated steel is significant and cannot be ignored. So it is necessary to inspect the corrugated steel in a timely manner and avoid reducing the structural strength of the corrugated steel due to defect problems.

### 3.4. Structural Response of Corrugated Steel with Reinforcement Under High Sea Conditions

By installing reinforcement components and applying unilateral pressure, the structural response of corrugated steel with reinforcement under high sea conditions can be simulated. Figure 18 shows the stress cloud map of the reinforced corrugated steel under uneven unilateral pressure of 1 bar. Under this pressure, the corrugated steel exhibits minimal strain and does not interact with the reinforcement. The overall stress distribution and magnitude of the reinforced corrugated steel are similar to those of the non-reinforced steel under the same uneven pressure.

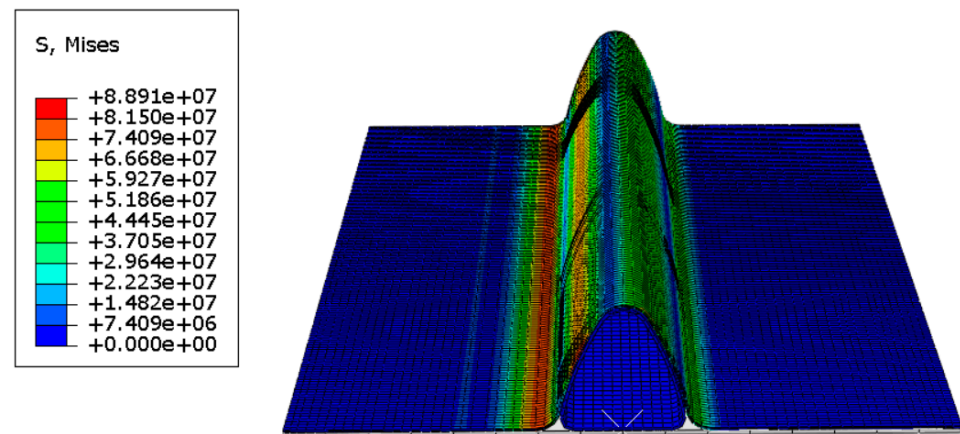


Figure 18. Stress cloud map of the reinforced model under non-uniform unilateral pressure of 1 bar.

Figure 19 shows the stress cloud map of the reinforced corrugated steel under non-uniform unilateral pressure of 3 bar. Under this pressure, the corrugated steel interacts with the reinforcement. Consequently, the reinforced steel model exhibits slightly lower stress than the non-reinforced steel under the same uneven pressure.

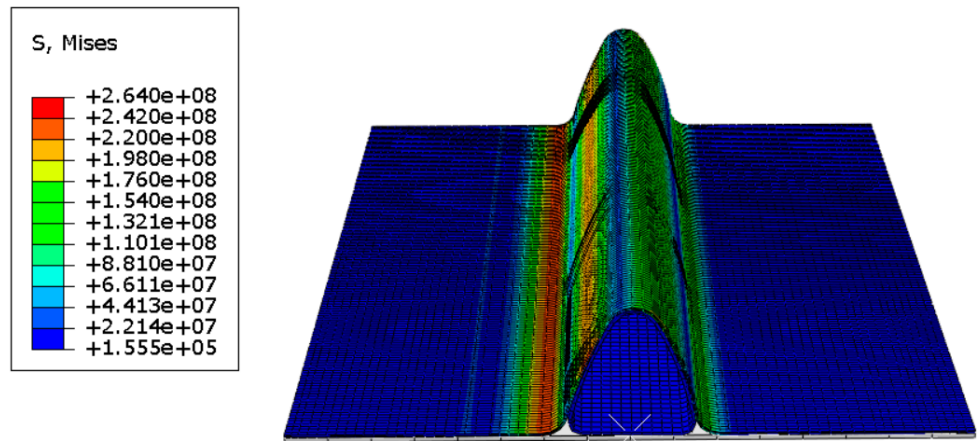


Figure 19. Stress cloud map of the reinforced model under non-uniform unilateral pressure of 3 bar.

Figure 20 shows the stress cloud map of the reinforced corrugated steel under a non-uniform unilateral pressure of 6 bar. Under this pressure, the stress in the corrugated steel increases, leading to stronger interactions between the corrugated steel and the reinforcement. Moreover, as the pressure increases, the reinforcement undergoes a more rapid increase in stress than the corrugated steel. Overall, the reinforced model exhibits slightly lower stress than the non-reinforced model under the same uneven pressure.

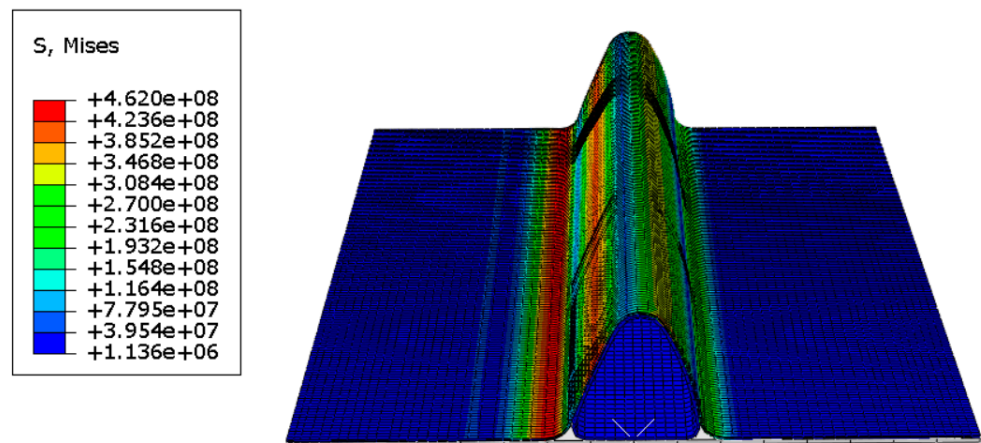
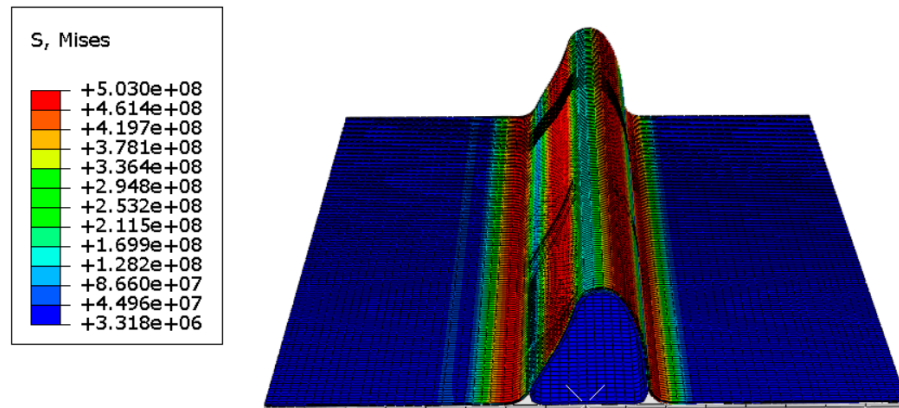


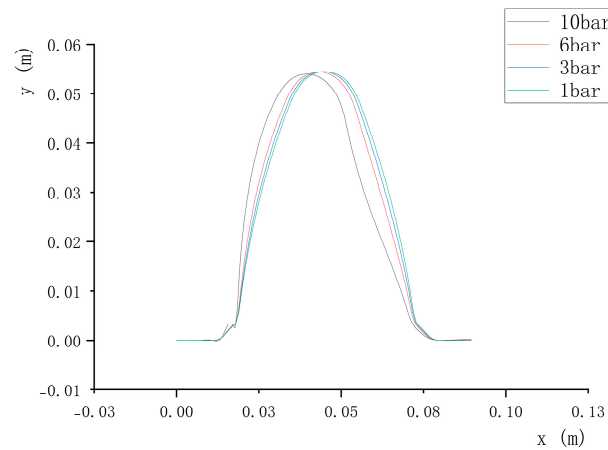
Figure 20. Stress cloud map of the reinforced model under non-uniform unilateral pressure of 6 bar.

Figure 21 shows the stress cloud map of the reinforced corrugated steel under a non-uniform unilateral pressure of 10 bar. Under this pressure, both the corrugated plate and reinforcement on the stressed side undergo significant deformation. The entire structure tilts toward the non-stressed side of the plate, and the curvature in the middle section of the corrugated plate on the stressed side decreases. Moreover, the reinforced model exhibits lower stress than the non-reinforced model under the same uneven pressure.



**Figure 21.** Stress cloud map of the reinforced model under non-uniform unilateral pressure of 10 bar.

Figure 22 shows the strain of the reinforced corrugated plate under different non-uniform loads. Under uneven loads, deformation mainly occurs in the middle, top, and transition areas below the stressed side of the reinforced corrugated plate. Consequently, the overall model tilts toward the non-stressed side of the plate. Additionally, the middle circular arc area of the reinforced corrugated plate decreases compared with the non-reinforced plate.



**Figure 22.** Strain of the reinforced model under different non-uniform unilateral pressures.

The structural reinforcement can enhance stability and reduce stress and strain. Under a pressure of 10 bar, the maximum stress of the corrugated plate with added reinforcement is 503 MPa, which is 5.1% lower than that of the corrugated plate without reinforcement (530.1 Mpa). Under a pressure of 10 bar, the corrugated steel without reinforcement components showed significant deformation, especially in the curved part, with signs of collapse. After installing the reinforcement, the deformation of the circular arc area in the middle of the corrugated steel is significantly reduced. It is worth noting that the reinforcement may not be able to completely resist the collapse of corrugated steel, but it can improve the compressive strength to a certain extent.

Different materials of reinforcement are compared. The maximum stress of the corrugated plate with added aluminum alloy reinforcement is 516 MPa, which is larger than that of the corrugated plate with stainless steel reinforcement, as listed in Table 3. Furthermore, from the perspective of corrosion, stainless steel is a more suitable material for reinforcement components, because if other different materials are selected, the electrode potentials of other materials are different from those of corrugated stainless steel, which can easily cause electrochemical corrosion.

**Table 3.** Comparison of different materials.

Materials	Maximum Stress (MPa)
Stainless steel	503
Aluminum alloy	516

Because the reinforcement is closely attached to the corrugated steel, the outline is fixed but the wall thickness can be changed. As the wall thickness increases, the maximum stress decreases, but the decrease is not significant, as shown in Table 4. When the wall thickness increases, the cost increases and the weight also increases. So, concerning the wall thickness, it is not necessarily the thicker the better; it needs to be considered comprehensively from the perspectives of economy and practicality.

**Table 4.** Comparison of different wall thickness.

Wall Thickness (mm)	Maximum Stress (MPa)
1.2	503
2	490
2.8	479

#### 4. Conclusions

In this work, the response behavior of the stainless steel inner wall structure in LNG ship membrane tanks was examined under high sea conditions. The characteristics of the inner wall structure were simulated under normal conditions, with defects, and with fasteners. The following conclusions were drawn:

(1) Under uniform loads, the corrugated steel exhibits relatively low stress and strains and maintains symmetry around the central axis. Conversely, under uneven loads, the corrugated steel features greater stress and strain, with early signs of initial yield. During high sea state conditions with liquid tank oscillation, the tank wall becomes more prone to yielding and deformation, thereby increasing the risk of accidents.

(2) In the presence of defects, the corrugated steel strip exhibits higher stress and strain under the same load. At a pressure of 10 bar, the defective corrugated steel exhibits a 2.3% increase in maximum stress and features an earlier, more pronounced initial yield than the defect-free steel.

(3) The incorporation of reinforcement into the corrugated plate reduces its stress and strain. Under a pressure of 10 bar, the reinforced corrugated plate features a maximum stress of 503 Mpa, which is 5.1% lower than that of the non-reinforced corrugated plate. Therefore, the addition of reinforcement to the back of the corrugated plate can improve its ability to resist uneven pressure.

In this work, a simple defect is analyzed by simulating damage as cylindrical displacements. In fact, there are various types of defects, such as lateral cracks, longitudinal cracks, non-uniform wear, pores, bulges, compositional defects, and so on. In the following research, we will consider various types of defects and research in detail the impact of different types of defects on the structure characteristics.

**Author Contributions:** Data curation, Y.Z.; investigation and methodology, Z.M. and P.G.; writing—original draft, F.D. All authors have read and agreed to the published version of the manuscript.

**Funding:** This research was funded by the Dalian High-level Talents Innovation Support Program, grant number 2020RQ129.

**Institutional Review Board Statement:** Not applicable.

**Informed Consent Statement:** Not applicable.

**Data Availability Statement:** Data are contained within the article.

**Conflicts of Interest:** The authors declare no conflicts of interest.

## References

1. Song, M.J.; Ahn, Y.J.; Kim, S.Y.; Kim, Y.; Jung, J.H.; Kim, J.H. Effects of sloshing loads on fatigue strength of independent type b lng tank. *Int. J. Offshore. Polar.* **2013**, *23*, 112–119.
2. Hu, Z.Q.; Zhang, D.W.; Zhao, D.Y.; Chen, G. Structural safety assessment for FLNG-LNGC system during offloading operation scenario. *China Ocean Eng.* **2017**, *31*, 192–201. [[CrossRef](#)]
3. Duong, P.A.; Ryu, B.R.; Jung, J.; Kang, H. A comprehensive review of the establishment of safety zones and quantitative risk analysis during ship-to-ship LNG bunkering. *Energies* **2024**, *17*, 512. [[CrossRef](#)]
4. Yuan, J.; Shi, X.P.; He, J.L. LNG market liberalization and LNG transportation: Evaluation based on fleet size and composition model. *Appl. Energy* **2024**, *358*, 122657. [[CrossRef](#)]
5. Li, Y.W.; Tian, W.L.; Meng, B.B.; Zhang, J.F.; Zhou, R.S. A simulation model of the influence of LNG ships on traffic efficiency at tianjin port. *J. Mar. Sci. Eng.* **2024**, *12*, 405. [[CrossRef](#)]
6. He, P.; Jin, J.G.; Pan, W.; Chen, J.H. Route, speed, and bunkering optimization for LNG-fueled tramp ship with alternative bunkering ports. *Ocean Eng.* **2024**, *305*, 117957. [[CrossRef](#)]
7. Jiao, J.L.; Zhao, M.M.; Jia, G.Y.; Ding, S. SPH simulation of two side-by-side LNG ships' motions coupled with tank sloshing in regular waves. *Ocean Eng.* **2024**, *297*, 117022. [[CrossRef](#)]
8. Kim, S.; Lee, J.G.; Kim, S.; Heo, J.; Bang, C.S.; Lee, D.K.; Lee, H.; Park, G.; Lee, D.; Lim, Y. Experiment and simulation of LNG self-pressurization considering temperature distribution under varying liquid level. *Energy* **2024**, *290*, 130071. [[CrossRef](#)]
9. Park, J.S.; Kim, J.H.; Jeong, Y.C.; Kim, H.T.; Kim, S.K.; Lee, J.M. Effect of corrugated sheet diameter on structural behavior under cryogenic temperature and hydrodynamic load. *Metals* **2022**, *12*, 521. [[CrossRef](#)]
10. Liu, J.F.; Feng, G.Q.; Wang, J.Y.; Ren, H.L.; Song, W.; Lin, P.P. Fatigue life assessment in the typical structure of large container vessels based on fracture mechanics. *J. Mar. Sci. Eng.* **2023**, *11*, 2075. [[CrossRef](#)]
11. Gaidai, O.; Storhaug, G.; Naess, A.; Ye, R.C.; Cheng, Y.; Xu, X.S. Efficient fatigue assessment of ship structural details. *Ships Offshore Struct.* **2019**, *15*, 503–510. [[CrossRef](#)]
12. Fricke, W. Fatigue and Fracture of Ship Structures. In *Encyclopedia of Maritime and Offshore Engineering*; Wiley: New York, NY, USA, 2017; pp. 1–12.
13. Ræstad, A.E.; Gjestland, T. Propeller- and Thruster-Induced Noise and Vibration. In *Encyclopedia of Maritime and Offshore Engineering*; Wiley: New York, NY, USA, 2017; pp. 1–14.
14. Dong, Y.; Garbatov, Y.; Guedes Soares, C. Review on Uncertainties in Fatigue Loads and Fatigue Life of Ships and Offshore Structures. *Ocean Eng.* **2022**, *264*, 112514. [[CrossRef](#)]
15. Xia, T.; Yang, P.; Li, C.; Hu, K. Numerical Research on Residual Ultimate Strength of Ship Hull Plates under Uniaxial Cyclic Loads. *Ocean Eng.* **2019**, *172*, 385–395. [[CrossRef](#)]
16. Corigliano, P.; Crupi, V.; Epasto, G.; Guglielmino, E.; Risitano, G. Fatigue assessment by thermal analysis during tensile tests on steel. *Ital. Group Fract. Meet.* **2015**, *109*, 210–218. [[CrossRef](#)]
17. Kim, B.G.; Lee, D.G. Leakage characteristics of the glass fabric composite barriers of LNG ships. *Compos. Struct.* **2008**, *86*, 27–36. [[CrossRef](#)]
18. Wang, X.; Arai, M. A study on coupling effect between seakeeping and sloshing for membrane-type LNG carrier. *Int. J. Offshore Polar.* **2011**, *21*, 256–263.
19. Kim, S.K.; Park, S.I.; Paik, J.K. Collision-accidental limit states-based safety studies for a LNG-fuelled containership. *Ocean Eng.* **2022**, *257*, 111571. [[CrossRef](#)]
20. Choi, T.; Park, J.; Bak, J.; Park, D.; Seo, H.; Kim, S.; Bi, G.J. The development of software to automate the laser welding of a liquefied natural gas cargo tank using a mobile manipulator. *Appl. Sci.* **2024**, *14*, 134. [[CrossRef](#)]
21. Jeong, H.; Shim, W.J. Calculation of boil-off gas (bog) generation of KC-1 membrane LNG tank with high density rigid polyurethane foam by numerical analysis. *Pol. Marit. Res.* **2017**, *24*, 100–114. [[CrossRef](#)]
22. Ju, H.B.; Jang, B.S.; Choi, J.; Yim, K.H.; Yang, Y.; Han, S. Structural safety assessment procedure for membrane-type LNG CCS considering hydroelasticity effect. *Mar. Struct.* **2021**, *78*, 102962. [[CrossRef](#)]
23. Wu, J.M.; Lv, L.W.; Cai, S.J. Research on the internal pressure of liquefied natural gas ship cargo tanks. *Shanghai Shipbuild.* **2011**, *85*, 37–42.
24. Fu, J.H. Analysis and calculation of internal pressure in thin film lng cargo tanks. *Jiangsu Ship* **2015**, *32*, 21–30. [[CrossRef](#)]
25. Kim, C.B.; Yoon, H.S.; Lee, G.D. Pressure resistance of the corrugated stainless steel membranes of LNG carriers. *Ocean Eng.* **2010**, *38*, 592–608. [[CrossRef](#)]
26. Sohn, J.M.; Bae, D.M.; Bae, S.Y.; Paik, J.K. Nonlinear structural behaviour of membrane-type LNG carrier cargo containment systems under impact pressure loads at  $-163\text{ }^{\circ}\text{C}$ . *Ship Offshore Struct.* **2017**, *12*, 722–733. [[CrossRef](#)]
27. Park, Y.I.; Kim, J.H. Artificial neural network based prediction of ultimate buckling strength of liquid natural gas cargo containment system under sloshing loads considering onboard boundary conditions. *Ocean Eng.* **2022**, *249*, 110981. [[CrossRef](#)]
28. Graczyk, M.; Berget, K.; Allers, J. Experimental investigation of invar edge effect in membrane LNG tanks. *J. Offshore. Mech. Arct.* **2012**, *134*, 031801. [[CrossRef](#)]
29. Yan, X.S.; Huang, X.P.; Huang, Y.C.; Cui, W.C. Prediction of fatigue crack growth in a ship detail under wave-induced loading. *Ocean Eng.* **2016**, *113*, 246–254. [[CrossRef](#)]

30. Dong, Y.; Frangopol, D.M. Incorporation of risk and updating in inspection of fatigue-sensitive details of ship structures. *Int. J. Fatigue* **2016**, *82*, 676–688. [[CrossRef](#)]
31. Li, X.X. Research on the Constitutive Model Parameters Identification of 304 Stainless Steel. Master's Thesis, Huazhong University of Science and Technology, Wuhan, China, 2012.

**Disclaimer/Publisher's Note:** The statements, opinions and data contained in all publications are solely those of the individual author(s) and contributor(s) and not of MDPI and/or the editor(s). MDPI and/or the editor(s) disclaim responsibility for any injury to people or property resulting from any ideas, methods, instructions or products referred to in the content.